Computers in Biology and Medicine 111 (2019) 103353

Contents lists available at ScienceDirect

Computers in Biology and Medicine

journal homepage: www.elsevier.com/locate/compbiomed

A three-dimensional cross-directional bilateral filter for edge-preserving noise reduction of low-dose computed tomography images

Katsuhiro Ichikawa[a,*], Hiroki Kawashima[a], Masato Shimada[b], Toshiki Adachi[b], Tadanori Takata[c]

[a] Faculty of Health Sciences, Institute of Medical, Pharmaceutical and Health Sciences, Kanazawa University, 5-11-80 Kodatsuno, Kanazawa, 920-0942, Japan
[b] Department of Radiology, University of Fukui Hospital, 23-3, Matsuokashimoaizuki, Eiheiji-cho, Yoshida-gun, Fukui, 910-1193, Japan
[c] Radiology Division, Kanazawa University Hospital, 13-1 Takara-machi, Kanazawa, 920-8641, Japan

ARTICLE INFO

Keywords:
Computed tomography
Noise reduction
Non local mean
Bilateral filter
Task-based transfer function
Noise power spectrum
System performance

ABSTRACT

Background: Image-based noise reduction techniques are useful because they can be applied across various computed tomography (CT) scanner models from different vendors, regardless of the iterative reconstruction availability. The purpose of this study was to propose a 3-dimensional cross-directional bilateral filter (3D-CDBF) and compare the edge-preserving noise reduction on low-dose CT images to a model-based iterative reconstruction (MBIR).

Methods: The 3D-CDBF comprises a bilateral filter and a smoothing filter applied in range filtering. The filtering process was applied with four iterations using empirically determined parameters that yielded the best tradeoff between noise reduction and edge preservation for a very low radiation dose of 2.5 mGy. In-plane and z-directional edge preservation performances for low-contrast rod phantoms (60 Hounsfield units) were compared to a clinically available MBIR and a conventional 3D bilateral filter (3D-BF), using task-based spatial resolution (task-based transfer function: TTF) and slice thickness. Moreover, the noise power spectra (NPS) were compared. Furthermore, performance was compared on abdominal CT images acquired from volunteers at 2.5 mGy (approved by our institutional review board).

Results: In phantom tests, 3D-CDBF provided 28.5% higher spatial resolution at 50%TTF compared to MBIR. Moreover, total NPS was lower, while the slice thickness (z-axis resolution) was slightly broader than that achieved by MBIR (0.99 mm vs. 0.92 mm). 3D-BF was inferior to both 3D-CDBF and MBIR in all measurements. Consistent with phantom results, 3D-CDBF significantly reduced noise on abdominal images compared to MBIR ($P < 0.001$), exhibiting better preservation of organ edges.

Conclusion: This 3D-CDBF may provide superior edge preserving noise reduction of low-dose CT images compared to currently available MBIR.

1. Introduction

The radiation dose required for computed tomography (CT) is much higher than that of general radiography; thus the associated cancer risk is an important concern [1]. To reduce the required dose, various iterative reconstruction (IR) techniques have been developed [2,3]. Among these, a model based iterative reconstruction (MBIR) has been reported to provide excellent clinical performances in low-dose CT imaging [2–4]. On the other hand, different image-based noise reduction techniques have been investigated, and recently several such processing systems have become commercially available. To our knowledge, however, only one of these systems (SafeCT, Medic Vision Imaging Solutions Ltd., Tirat Carmel, Israel) has been scientifically evaluated, which demonstrated acceptable capability on half-dose scans [5–7]. Recently, the potential utility of image-based noise reduction using a convolutional neural network trained to convert low-dose CT images into routine dose-like images was reported [8–10]. The main advantage of these image-based techniques is that it can be applied to images acquired using different CT systems, unlike iterative reconstruction algorithms.

Techniques for image-based edge-preserving noise reduction such as the non local mean (NLM) [11] and the bilateral filter (BF) [12] have been widely used in general photography. NLM performs a weighted average using pixels in a search window (SW) around the center pixel,

* Corresponding author. Faculty of Health Sciences, Institute of Medical, Pharmaceutical and Health Sciences, Kanazawa University, Zip-code: 920-0942, 5-11-80 Kodatsuno, Kanazawa, Japan.
E-mail addresses: ichikawa@mhs.mp.kanazawa-u.ac.jp (K. Ichikawa), kawa3@med.kanazawa-u.ac.jp (H. Kawashima), mshima@u-fukui.ac.jp (M. Shimada), adachit@u-fukui.ac.jp (T. Adachi), t-takata@med.kanazawa-u.ac.jp (T. Takata).

https://doi.org/10.1016/j.compbiomed.2019.103353
Received 21 May 2019; Received in revised form 6 July 2019; Accepted 7 July 2019

based on the similarity of patches at the center pixel and each pixel in SW. Although NLM has been reported to be effective to reduce the CT image noise [13–15], it was evaluated to often produce an organized noise pattern artifact which could significantly compromise image quality and diagnosis, and such artifacts are observed in figures in previous papers [13,15]. BF achieves edge-preserving noise reduction by combining a Gaussian spatial filter (domain filter) and a range filter determining weighting factors according to value differences between a center pixel and neighboring pixels. However, there are few investigations of BF utility for CT images [15], possibly due to limited performance on speckle noise [16,17].

The purpose of this study was to develop and evaluate a 3-dimensional (3D) BF using cross-directional filtering between the BF and a smoothing filter applied in range filtering (3D cross-directional BF: 3D-CDBF), which improves the performance of BF for speckle noise. The filtering performance on low-dose CT images was compared to a clinically available MBIR.

2. Methods and materials

2.1. Three-dimensional bilateral filter with low-pass filtering

We used a 3D BF defined as,

$$g(i,j,k)=\frac{\sum_{n=-N_z}^{N_z}\sum_{m=-N_p}^{N_p}\sum_{l=-N_p}^{N_p} f(i+l,j+m,k+n)W_d(l,m,n)W_r(i,j,k,l,m,n)}{\sum_{n=-N_z}^{N_z}\sum_{m=-N_p}^{N_p}\sum_{l=-N_p}^{N_p} W_d(l,m,n)W_r(i,j,k,l,m,n)}, \quad (1)$$

where $f(i, j, k)$ is a voxel of volume data constructed from a stack of axial CT images, $g(i, j, k)$ is the corresponding processed voxel. The in-plane and z-directional kernel sizes are $(2N_p+1) \times (2N_p+1)$ and $2N_z+1$, respectively. W_d and W_r denote weighting factors for the domain and range filtering, respectively, and are calculated as follows:

$$W_d(l,m,n)=\exp\left(-\frac{l^2+m^2}{2{\sigma_{dp}}^2}\right)\exp\left(-\frac{n^2}{2{\sigma_{dz}}^2}\right), \quad (2)$$

$$W_r(i,j,k,l,m,n)=\exp\left(-\frac{(f_{LPF}(i,j,k)-f_{LPF}(i+l,j+m,k+n))^2}{2{\sigma_r}^2}\right), \quad (3)$$

where σ_{dp}, σ_{dz}, and σ_r are the standard deviations of in-plane, z-directional, and range Gaussian functions, respectively, adjusted to control noise reduction (σ_{dp} and σ_{dz}) and edge preservation (σ_r). σ_r is expressed in Hounsfield units (HU). This process basically requires an isotropic or near isotropic 3D data comprising consecutive CT images with slice intervals equivalent to the in-plane pixel pitch such that the in-plane and z-directional parameters can be set with an equal scale, thus allowing for the 3D filtering to work properly with the given parameters. For example, adult abdominal CT images (field of view sizes of $300-400$ mm with a matrix size of 512×512) with a thin slice thickness less than 1.0 is generally suitable.

The main difference from conventional BF is that the weighting factor for the range filter is calculated from low-pass-filtered volume data [$f_{\mathrm{LPF}}(i, j, k)$] processed with a 3D Gaussian-type filter using waiting factor W_{LPF} calculated as,

$$W_{LPF}(l,m,n)=\exp\left(-\frac{l^2+m^2}{2{\sigma_{LPFp}}^2}\right)\exp\left(-\frac{n^2}{2{\sigma_{LPFz}}^2}\right),$$

where σ_{LPFp} and σ_{LPFz} are standard deviations that control the in-plane and z-directional filtering, respectively.

2.2. Cross-directional method

The weakness of BF for speckle noise reduction is caused by the range filtering, as extreme pixel values generated by noise are preserved because of high weighting in range filtering. An alternative for improved noise filtering is to calculate W_r from $f_{\mathrm{LPF}}(i, j, k)$, a low-pass filtered version of $f(i, j, k)$. This idea is similar to the joint BF proposed by Petschnigg et al. [18], where a noisy photograph acquired without a flash is corrected using weighting factors for range filtering calculated from a photograph taken with a flash. However, in the case where data used for the weighting factor calculation is not acquired using a sufficient radiation dose but is rather a blurred image (i.e., f_{LPF}), noise can be reduced but edge preservation is impossible. To address this limitation, we devised a method to cross the filtering directions (1) between a BF with a z-directional 3D kernel with $\sigma_{dp} \ll \sigma_{dz}$ and an in-plane LPF applied for producing f_{LPF} (i.e., $\sigma_{LPFp} \gg \sigma_{LPFz}$), and (2) between a BF with an in-plane 3D kernel with$\sigma_{dp} \gg \sigma_{dz}$ and a z-directional LPF for f_{LPF} ($\sigma_{LPFp} \ll \sigma_{LPFz}$). Each LPF works to reduce the speckle noise, and edge blurring is also suppressed because the edge preservation of BF is performed in the direction orthogonal to that of LPF. The noise reduction was iteratively processed based on these two types of 3D-CDBF as described in the next section.

2.3. Iteration of cross-directional bilateral filtering

The 3D-CDBF is performed with two to six iterations. At first, a 3D-CDBF with $\sigma_{dp} \ll \sigma_{dz}$ and $\sigma_{LPFp} \gg \sigma_{LPFz}$ (z-dominant 3D-CDBF: 3D-CDBF$_Z$) is applied. The processing is iteratively repeated with varying σ_{dp}, σ_{dz}, σ_{LPFp} and σ_{LPFz}, where σ_{dp} linearly increases toward the initial σ_{dz} value, σ_{dz} decreases linearly toward the initial σ_{dp} value, σ_{LPFp} linearly changes from a large value (σ_{LPFp1}) to a small value (σ_{LPFp2}), and σ_{LPFz} changes from a small value (σ_{LPFz1}) to a large value (σ_{LPFz2}). Finally, a 3D-CDBF with $\sigma_{dp} \gg \sigma_{dz}$ and $\sigma_{LPFp} \ll \sigma_{LPFz}$ (in-plane dominant 3D-CDBF: 3D-CDBF$_{xy}$) was applied. The σ_r for the range filtering is set to a constant value such that edges are preserved on objects with contrasts $> \sigma_r$. These parameter transitions are summarized in Table 1. We preliminarily investigated several iteration (parameter-change) methods to obtain better 3D isotropic properties of both noise reduction and edge preservation. Consequently, the method that starts with $\sigma_{dp} \ll \sigma_{dz}$ and then linearly changes the parameters was empirically found to give a superior 3D isotropic appearance. Although the fewer iterations can be selected when the lower noise is included, at least two iterations are needed for z-directional ($\sigma_{dp} \ll \sigma_{dz}$) and subsequent in-plane ($\sigma_{dp} \gg \sigma_{dz}$) bilateral filtering.

Similar to conventional BF, the σ_{dp} and σ_{dz} parameters control noise reduction for the in-plane and z-direction, respectively. The σ_r parameter controls edge preservation. Moreover, in 3D-CDBF, σ_{LPFp} andσ_{LPFz} were modified empirically to suppress the remaining speckle noise. Although a larger σ_{LPF} is more effective for speckle noise suppression, we experienced that an excessive σ_{LPF} larger than 3.0 tends to reduce the pixel intensities of some fine structures, while most of the object edges are preserved.

Table 1
Parameter transition summary for the iteration process of our proposed 3D cross-directional bilateral filter (3D-CDBF). Values in parentheses are the baseline parameters used in this study.

	Iteration step	
	First	Last (4th)
σ_{dp}	Small (0.40)	Large (2.00)
σ_{dz}	Large (2.00)	Small (0.40)
σ_{LPFp}	Large (3.00)	Small (0.38)
σ_{LPFz}	Small (0.38)	Large (1.50)
σ_r (HU)	Constant (10)	

2.4. Blending process

Since the noise reduction of 3D-CDBF is achieved by combining different Gaussian LPFs, a texture change and consequent "unnatural" look are unavoidable. Thus, we blended the filter back projection (FBP) images, which is a widely used method to improve the unnatural look of images [19,20], as a final processing step. The blending rate was set to 30%.

2.5. Noise reduction performance evaluation

2.5.1. Phantom

Edge-preserving noise reduction was evaluated using the task-based modulation transfer function (task transfer function: TTF) [21] and noise power spectrum (NPS). In general, the spatial resolution of conventional CT images reconstructed by FBP can be measured from a point spread function image obtained by scanning a thin metal wire because FBP is a linear process and thus high contrast (e.g., more than 1000 HU) does not preclude accurate measurements [22]. However, the spatial resolutions of IR and BF images vary depending on image noise and contrast because these processes are non-linear processes. Thus, a task-based method using objects with specific contrasts (CT-numbers) is more suitable for evaluating the spatial resolution of clinical images processed by IR and BF [21].

Fig. 1 is a schematic of the cylindrical water-filled phantom used in the first stage of 3D-CDBF evaluation. The outer diameter was 200 mm, and a rod object with a diameter of 30 mm and height of 40 mm was placed into the phantom as shown in the figure. Disk images of the rod were used for measuring TTF. This phantom design was adopted to simulate the American College of Radiology (ACR) CT accreditation phantom previously employed for evaluating TTF of IR techniques [21,23]. Previous studies have reported that the TTF of IR is degraded with decreasing of object contrast [21,23], and the lowest contrast obtained with the acrylic rod insert of the ACR phantom is ~120 HU at the generally used X-ray tube voltage of 120 kV. In this study, we employed an even lower contrast of 60 HU (i.e., a more rigorous task) because the edge information of objects with such low contrast is important when evaluating detailed lesion structures such as plaques in coronary arteries and deep venous thromboses [22,24]. The rod was made of a soft tissue-equivalent material (SZ-207, Kyoto Kagaku, Kyoto, Japan) with a CT number of ~58 HU at 120 kV. The NPS was measured from uniform images of the water-only volume as shown in Fig. 1.

For evaluating the effect of the denoising processes on slice thickness, another rod object made of the same soft-tissue-equivalent material with 70 mm diameter and 20 mm height was placed in the 200-mm cylindrical water phantom at an inclination of approximately 6° relative to the rotational axis (Fig. 2). As shown in Fig. 2, sagittal images were reconstructed from the axial image stack and then averaged into a single sagittal image to reduce image noise. This low-noise sagittal image was used to measure the task-based slice thickness as described in a later section (*2.5.3*). No interpolation was applied in the sagittal image reconstruction to measure accurate slice thickness.

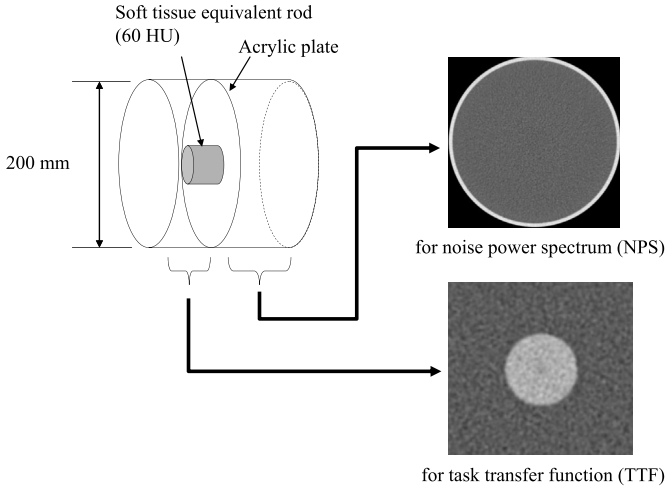

Fig. 1. Illustration of the phantom used for task-based transfer function (TTF) and noise power spectrum (NPS) measurements and example axial images used for TTF and NPS analyses.

2.5.2. Data acquisition and reconstruction method

All images were acquired using a Discovery CT750HD multi-slice CT scanner (GE Healthcare GE Healthcare, Milwaukee, WI, USA) with scan parameters 120 kV, 65 mA, 0.5 s/rotation, pitch factor of 0.984, and 64 × 0.625 mm detector configuration. The corresponding volume CT dose index ($CTDI_{vol}$) was 2.5 mGy, which is one tenth of the guidance dose (25 mGy) for the adult abdomen according to the International Atomic Energy Agency [25]. CT images were reconstructed with an FBP and MBIR (Veo, GE Healthcare) implemented in the CT scanner. For both FBP and MBIR reconstructions, the nominal slice thickness and slice interval were both set to 0.625 mm and a display field-of-view (DFOV) setting of 200 mm was used. A "Standard" reconstruction kernel was used for FBP. The MBIR (Veo) requires a much longer reconstruction time (> 30 min per acquired volume) because it performs a full version IR involving multiple iterations between projection space and image space [26].

In general, a low-dose acquisition produces greater image noise, thus precluding accurate measurement of TTF. To overcome this problem, several studies have used the image averaging technique with many consecutive rod images [7,22,27]. In this study, the phantom scan was repeated four times to obtain a total of 200 images for averaging (50 images per one scan). Accordingly, we carefully placed the phantom such that the central axes of the soft-tissue-equivalent rod were precisely parallel to the rotational axis of the CT system.

For measurement of task-based slice thickness, the phantom scan was repeated three times, and the three images at each slice location were averaged. From an axial image stack constructed with the averaged axial images, a sagittal image including an inclined edge image was obtained by horizontal averaging (Fig. 2).

2.5.3. Data analysis

From the circular edge of the averaged rod image, a one-dimensional (1D) edge spread function (ESF) was obtained using the previously reported circular edge technique for measuring TTF [21]. The bin width used to create equidistant oversampled ESF data and simultaneously reduce noise was set to one fifth of the pixel pitch corresponding to the 200-mm DFOV (0.39 mm/5 = 0.078 mm). The synthesized ESF was differentiated to yield the line spread function, and then the dataset size was increased to 256 points using a zero-padding technique to enable a fast Fourier transform calculation.

Task-based slice thickness was measured from the averaged sagittal image of the tilted rod object. A synthesized edge profile was obtained using an established method to derive a synthesized edge profile from an image of a slanted edge [28]. Because the inclination angle was ~6°, we were able to obtain sufficiently small data intervals (~0.06 mm) through the synthesizing operation. The slice sensitivity profile (SSP) was calculated by differentiation of the synthesized edge profile [29]. We determined the full-width at half maximum (FWHM) of SSP to define the task-based slice thickness. Moreover, the TTF in z-direction was calculated from the obtained task-based SSP using a one-dimensional Fourier transformation with 256-point data generated through the zero-padding process.

The NPS was measured from uniform images of the water-only volume shown in Fig. 1, using 2D Fourier transform [7,23,24]. NPS results of 200 images were averaged to almost completely eliminate the statistical error of the NPS measurement. The region of interest (ROI) size was set to 128 × 128 pixels at the center of image.

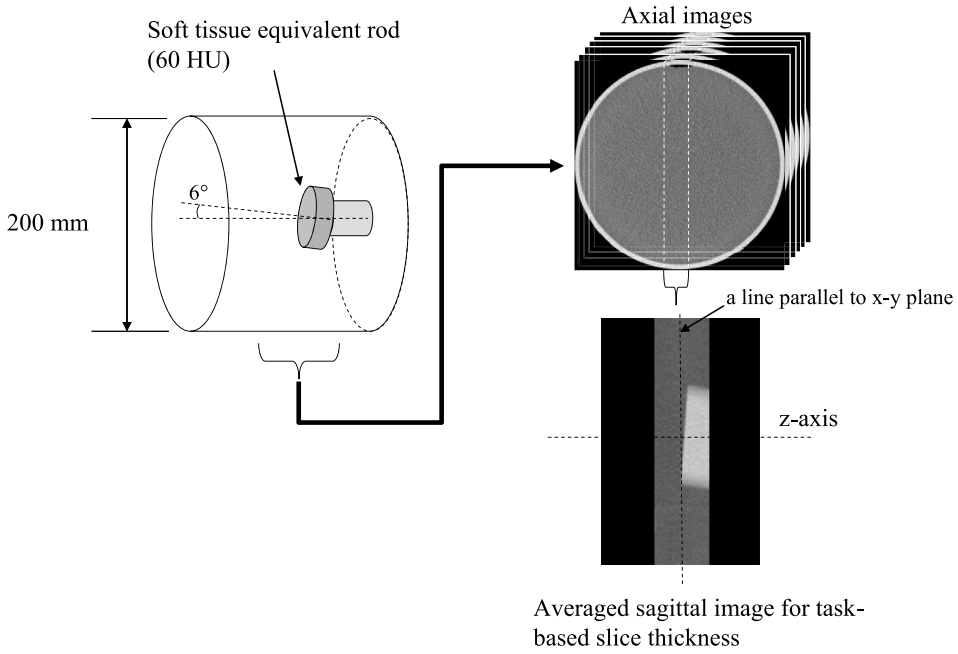

Fig. 2. Illustration of phantom used for task-based slice thickness (task-based slice sensitivity profile: task-based SSP) measurement and an outline of the process for producing an averaged sagittal image for analyzing the z-directional edge profile.

2.5.4. System performance function

A previous study investigating imaging performance of IR techniques [23] used the following detectability index d' to assess imaging performance:

$$d'^2 = \int \frac{TTF^2(u)}{NPS(u)} S^2(u)du, \tag{4}$$

where u denotes the spatial frequency and $S(u)$ is the spectrum of the signal to be detected. The d'^2 value incorporates the square of system performance (SPF) $TTF^2(u)/NPS(u)$ and imaging task $S^2(u)$ [23,30]. This index is similar to the pre-whitening signal-to-noise ratio based on an ideal observer model [30]. In this study, we focused on this SPF, expressed as

$$SPF^2(u) = \frac{TTF^2(u)}{NPS(u)}, \tag{5}$$

to compare edge-preserving noise reduction as a function of spatial frequency [7].

2.5.5. Processing parameters of 3D-CDBF

The processing parameters of 3D-CDBF for four iterations were $\sigma_{dp} = 0.4$, $\sigma_{dz} = 2.0$, $\sigma_{LPFp1} = 3.0$, $\sigma_{LPFp2} = 0.38$, $\sigma_{LPFz1} = 0.38$, $\sigma_{LPFz2} = 1.5$, and $\sigma_r = 10$ HU. As mentioned earlier, in the iteration process, σ_{dp} is linearly increased toward the initial σ_{dz} value, and σ_{dz} is decreased linearly toward the initial σ_{dp} value. These parameters were determined as a baseline parameter set empirically to achieve the best tradeoff between noise reduction and edge preservation at the low dose of 2.5 mGy. As mentioned earlier, since σ_{dp} and σ_{dz} control noise reduction, and σ_r controls edge preservation, their effects are understandable, corresponding to the basic properties of BF. However, the effect of LPF in the cross-directional filtering on the edge-preservation is unclear because of the novel filtering method that was introduced in this study. Therefore, we investigated the effect of σ_{LPFp1} (for the in-plane LPF in the first iteration) on all measurements using σ_{LPFp1} of 6.0, 3.0 (baseline), and 1.5, and the effect of σ_{LPFz2} (for the z-directional LPF in the final iteration) using σ_{LPFz2} of 3.0, 1.5 (baseline), and 0.75. The baseline parameters were also used except for each investigated parameter. In addition, we processed the FBP image using a conventional 3D bilateral filter (3D-BF) using parameters of $\sigma_{dp} = 2.0$, $\sigma_{dz} = 2.0$, and $\sigma_r = 100$ HU, with no LPF for range filtering and no iteration. The σ_{dp} and σ_{dz} values were selected in accordance with the initial σ_{dz} (= final σ_{dp}) value of 3D-CDBF. The large σ_r value of 100 HU was needed to obtain a sufficient noise reduction, at the cost of degradation of edge-preserving. The iteration process was not applied because we found that the image appearance became severely unnatural.

2.6. Low-dose abdominal CT

Upper abdominal CT scans were acquired for two volunteers using the same $CTDI_{vol}$ of 2.5 mGy on a Discovery CT750HD system. The image acquisition protocol was approved by our institutional review board. The corresponding effective dose ~0.5 mSv is within the second lowest level of volunteer exposure designated by International Commission on Radiological Protection (ICRP) Publication 103, which classifies volunteer exposure into four levels according to benefits to society from "minor" (< 0.1 mSv) to "substantial" (> 10 mSv) [31]. The scan and reconstruction parameters were the same as those of the phantom experiments, except that DFOV was 350 mm to include axial slices of the abdomen. The image noise was evaluated by the standard deviation (SD) of 30 × 30 pixel ROIs placed on regions of liver parenchyma with no visible objects such as vessels or cysts. Ten slices with 5-slice intervals were selected for each case, and three ROIs were placed on each slice to obtain 30 SD values. These 30 SD values were averaged and compared between MBIR and 3D-CDBF by Student's t-test for each volunteer case. In addition to the baseline parameters, we performed 3D-CDBF processing using σ_{LPFp1} of 6.0 and 1.5 and σ_{LPFz2} of 3.0 and 0.75, corresponding to the phantom analysis.

3. Results

3.1. Task transfer function

Fig. 3a shows the TTF values for FBP, MBIR, 3D-CDBF, and 3D-BF. The 50%TTF values were 0.38 mm^{-1} using FBP, 0.28 mm^{-1} using MBIR, 0.36 mm^{-1} using 3D-CDBF, and 0.27 mm^{-1} using 3D-BF, while corresponding 10%TTF values were 0.67, 0.56, 0.72 mm^{-1}, and 0.50 mm^{-1}, respectively. Thus, compared to MBIR, 3D-CDBF provided 28.5% higher spatial resolution at 50%TTF and 28.6% higher spatial

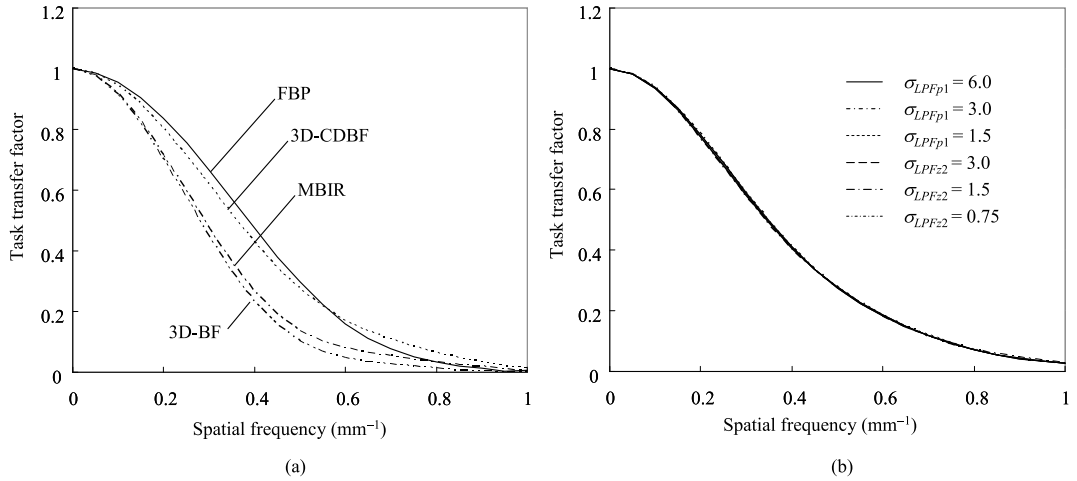

Fig. 3. Task-based transfer function (TTF) measurements (a) using FBP, MBIR, 3D-CDBF, and 3D-BF, and (b) using 3D-CDBF with σ_{LPFp1} of 6.0, 3.0 (baseline), 1.5 and σ_{LPFz2} of 3.0, 1.5 (baseline), 0.75. The baseline parameter set of 3D-CDBF for four iterations comprised σ_{dp} = 0.4, σ_{dz} = 2.0, σ_{LPFp1} = 3.0, σ_{LPFp2} = 0.38, σ_{LPFz1} = 0.38, σ_{LPFz2} = 1.5, and σ_r = 10 HU, and process parameters of 3D-BF was σ_{dp} = 2.0, σ_{dz} = 2.0, and σ_r = 100 HU with no iteration.

resolution at 10%TTF, indicating superior edge-preserving performance, even for the rigorous test condition of low (60 HU) contrast. 3D-BF indicated a slightly lower TTF than of MBIR. Fig. 3b shows TTFs of 3D-CDBF with σ_{LPFp1} of 6.0, 3.0 (baseline), and 1.5 and σ_{LPFz2} of 3.0, 1.5 (baseline), and 0.75. TTF was not affected by the σ_{LPFp1} and σ_{LPFz2} values tested.

3.2. Noise power spectrum comparison

Fig. 4a shows the NPS results for each method. Compared to FBP, MBIR significantly reduced the noise power, especially for middle frequencies. The noise power of MBIR and 3D-CDBF relative to FBP were 59.4% and 23.8%, respectively, at 0.1 mm^{-1} and 6.5% and 9.1%, respectively, at 0.5 mm^{-1}. 3D-CDBF reduced the noise power over the entire frequency range (not just for mid-range frequencies). The total noise reduction performance of 3D-CDBF was superior to MBIR. Although 3D-BF reduced the noise power from that of FBP, the performance was inferior to those of MBIR and 3D-CDBF. Fig. 4b shows NPSs of 3D-CDBF with σ_{LPFp1} of 6.0, 3.0 (baseline), and 1.5 and σ_{LPFz2} of 3.0, 1.5 (baseline), and 0.75. Most of $\sigma_{LPFp1}$and all of σ_{LPFz2}, we tested, did not affect to NPS, whereas only σ_{LPFp1} of 1.5 indicated a higher NPS in the low and middle frequency ranges (up to 0.5 mm^{-1}).

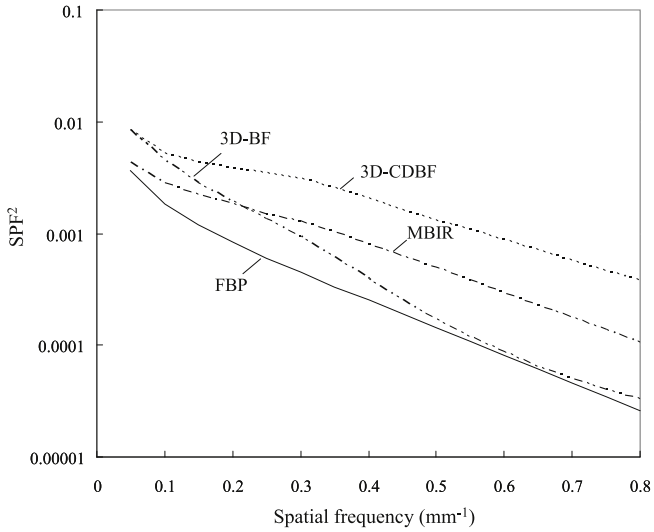

Fig. 5. Calculated system performance function (SPF) using TTF and NPS results of FBP, MBIR, 3D-CDBF with the baseline parameter set, and 3D-BF.

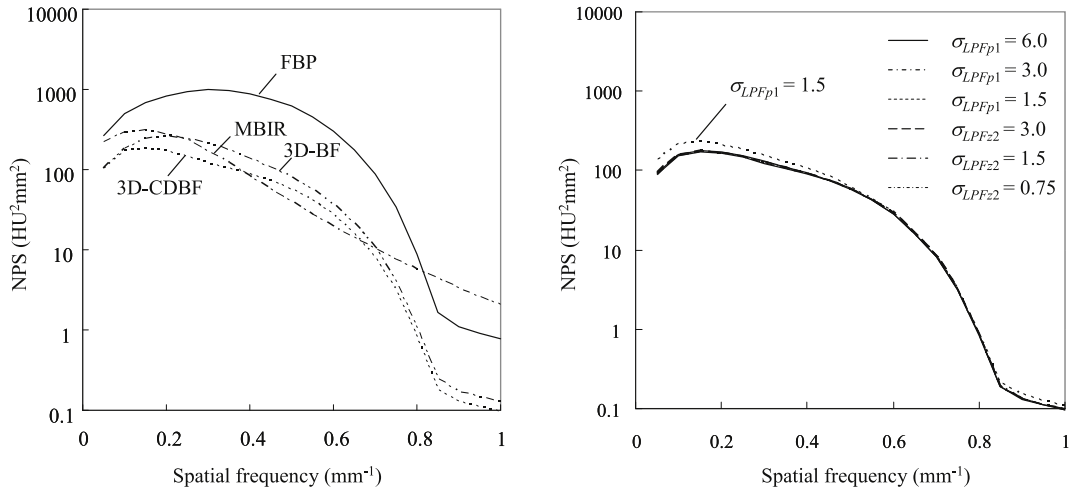

Fig. 4. Noise power spectra measured (a) using FBP, MBIR, 3D-CDBF with the base line parameter set, and 3D-BF, and (b) using 3D-CDBF with σ_{LPFp1} of 6.0, 3.0 (baseline), and 1.5 and σ_{LPFz2} of 3.0, 1.5 (baseline), and 0.75.

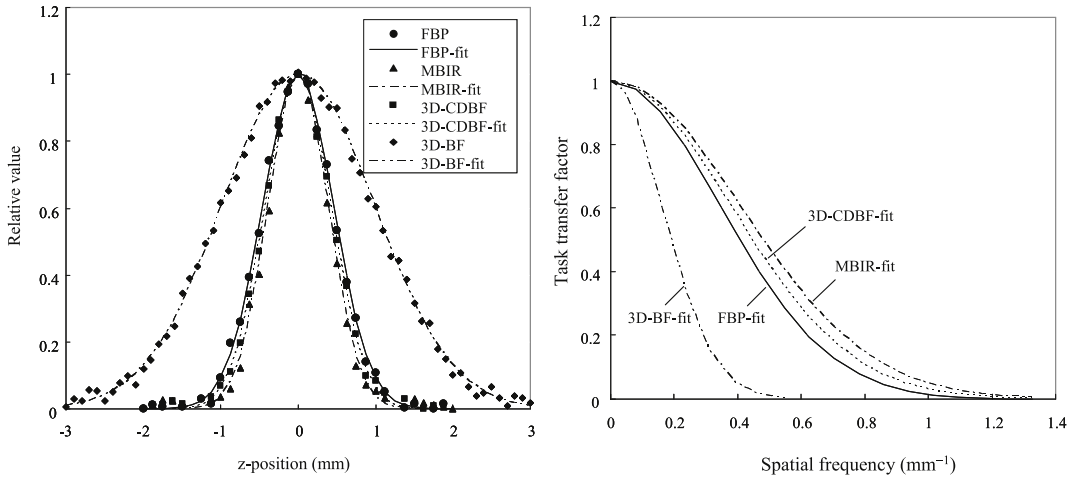

Fig. 6. Measured task-based SSP and z-directional TTF using FBP, MBIR, 3D-CDBF with the baseline parameter set, and 3D-BF.

3.3. System performance function comparison

The SPF^2 of 3D-CDBF with the baseline parameter set was significantly higher than that of MBIR (Fig. 5). The SPF^2 improvements at $0.1\,mm^{-1}$ relative to FBP were 54.3% using MBIR and 186.3% using 3D-CDBF, while the corresponding SPF^2 improvements at $0.5\,mm^{-1}$ were 243.4% and 828.3%, respectively. Therefore, 3D-CDBF improved SPF^2 by 84.8% at $0.1\,mm^{-1}$ and by 170.5% at $0.5\,mm^{-1}$ compared to MBIR, indicating substantially better edge-preserving noise reduction. 3D-BF was better than MBIR only at low frequencies $< 0.2\,mm^{-1}$, but mostly inferior to MBIR.

3.4. Task-based slice thickness

Fig. 6 shows measured results of the task-based SSP and z-directional TTF. A Gaussian fitting was applied to the resultant plots. The FWHM values obtained from the fitted results of FBP, MBIR, 3D-CDBF, and 3D-BF were 1.09, 0.92, 0.99, and 2.33 mm, respectively. The 50%TTF values of FBP, MBIR, 3D-CDBF, and 3D-BF were 0.41, 0.48, 0.45, and $0.19\,mm^{-1}$, respectively. 3D-BF presented a significantly broader SSP. Although MBIR yielded the best z-directional spatial resolution (slice thickness), there was only a slight difference between MBIR and 3D-CDBF (0.07 mm and $0.03\,mm^{-1}$). FWHM values for σ_{LPFz2} of 3.0 and 0.75 were 1.00 and 0.99 mm, respectively, while those of σ_{LPFp1} of 6.0 and 1.5 were 1.00 and 0.99 mm, respectively. Both the σ_{LPFz2} and σ_{LPFp1} parameters did not mostly affect to the task-based SSP.

3.5. Performance on low-dose abdominal CT images

Figs. 7 and 8 compare abdominal axial images and coronal multi-planar reformation (MPR) images between FBP, MBIR, 3D-CDBF, and 3D-BF for cases 1 and 2, respectively. A bilinear interpolation technique was used in the MPR process. The SD values of cases 1 and 2 were 38.5 ± 1.87 and 39.1 ± 1.91, respectively, using FBP, 12.6 ± 0.8 and 13.5 ± 0.9, respectively, using MBIR, 9.6 ± 0.5 and 10.2 ± 0.7, respectively, using 3D-CDBF, and 15.5 ± 1.1 and 16.8 ± 1.3, respectively, using 3D-BF. Values differed significantly between MBIR and 3D-CDBF for both cases ($P < 0.001$) and image noise was more effectively reduced by 3D-CDBF than by MBIR. Moreover, as shown in the magnified images of Fig. 9, organ and vessel edges were clearer on 3D-CDBF-processed images compared to MBIR-processed images as some sections of the organ edge on MBIR-processed images exhibited blush-like patterns (arrows in Fig. 9), which substantially limited resolution. Fig. 10 shows images processed using 3D-CDBF without and with the 30% blending of FBP images. Although 3D-CDBF itself caused substantial changes in noise texture, the blending process helped make the image texture natural.

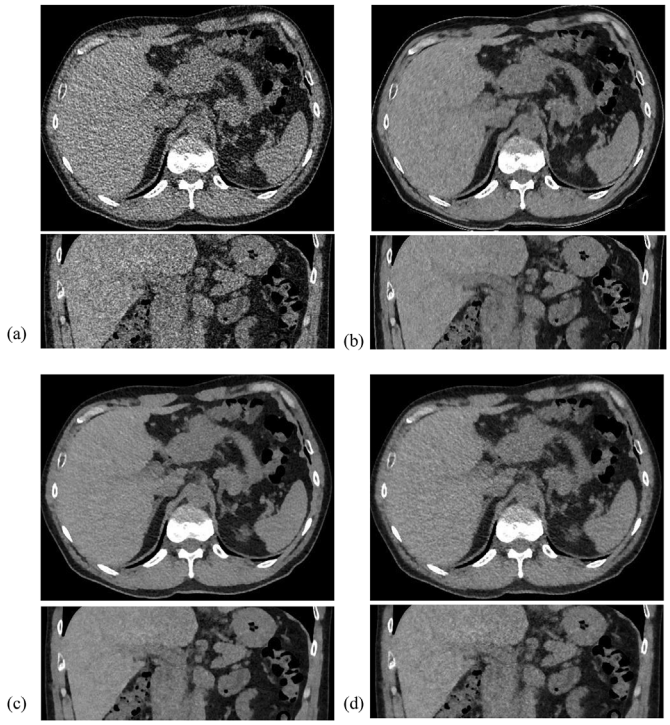

Fig. 7. Axial and coronal multi-planar reformation (MPR) images of volunteer case 1 for (a) FBP, (b) MBIR, (c) 3D-CDBF with the baseline parameter set, and (d) 3D-BF.

Fig. 11 shows axial and coronal reformation images of volunteer case 1, which were processed by 3D-CDBF with different σ_{LPFp1} settings. Increasing σ_{LPFp1} effectively reduced speckle noise, preserving object edges. However, the largest σ_{LPFp1} (6.0) exhibited lower pixel intensities at a thin intestine wall, compared to the others (arrows in the figure). Fig. 12 presents axial and coronal 3D-CDBF images of the volunteer case 1, which were processed with different σ_{LPFz2} settings (σ_{LPFz} at the final iteration). Corresponding to the NPS, TTF, and task-based SSP results showing almost no differences, the three images appear to be identical.

4. Discussion

We described a processing method of 3D-CDBF and superior edge-preserving noise reduction performance compared to MBIR. The 3D-

Fig. 8. Axial and coronal MPR images of volunteer case 2 for (a) FBP, (b) MBIR, (c) 3D-CDBF the baseline parameter set, and (d) 3D-BF.

CDBF method reduced image noise more effectively than MBIR and 3D-BF. The edge preservation as evaluated by TTF was also superior to MBIR and 3D-BF, with almost no alteration in TTF compared to FBP. Moreover, the performance evaluated by SPF indicated the superiority of 3D-CDBF over the entire frequency range. The processed low-dose CT images of volunteers also exhibited lower noise and clearer organ edges using 3D-CDBF compared to MBIR and 3D-BF. The better overall noise reduction suppressing speckle noise was achieved by the LPF applied in

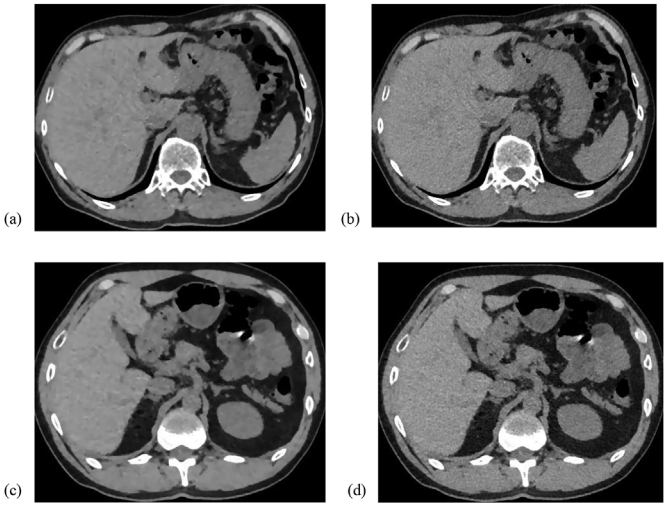

Fig. 10. 3D-CDBF images (a, c) without and (b, d) with 30% blending of FBP images for the volunteer case 1 (a, b) and case 2 (c, d).

the W_r calculation, while the excellent edge preservation was achieved by the cross-directional filtering, which is the defining feature of 3D-CDBF. Regarding the intermediate steps in four iteration, in the second (third) iteration, the difference between σ_{dp} and σ_{dz} becomes smaller than that of the first (last) iteration, and thus the effect of cross-directional filtering may be weakened. However, the smoothing parameter σ_{LPFp} (σ_{LPFz}) is also decreased from the first (last) value; as a result, the edge preservation performance was not degraded as demonstrated in the TTF and slice thickness results. Although the edge preservation was evaluated for only in-plane and z-direction, we presume that intermediate property between in-plane and z-directional properties were given through the iteration process because the coronal reformation images presented no discontinuities.

In both phantom and abdominal images, the nominal slice thickness was 0.625 mm, while the actual measured value was ~1.0 mm. In the clinical setting, it is generally difficult to use such thin slices with

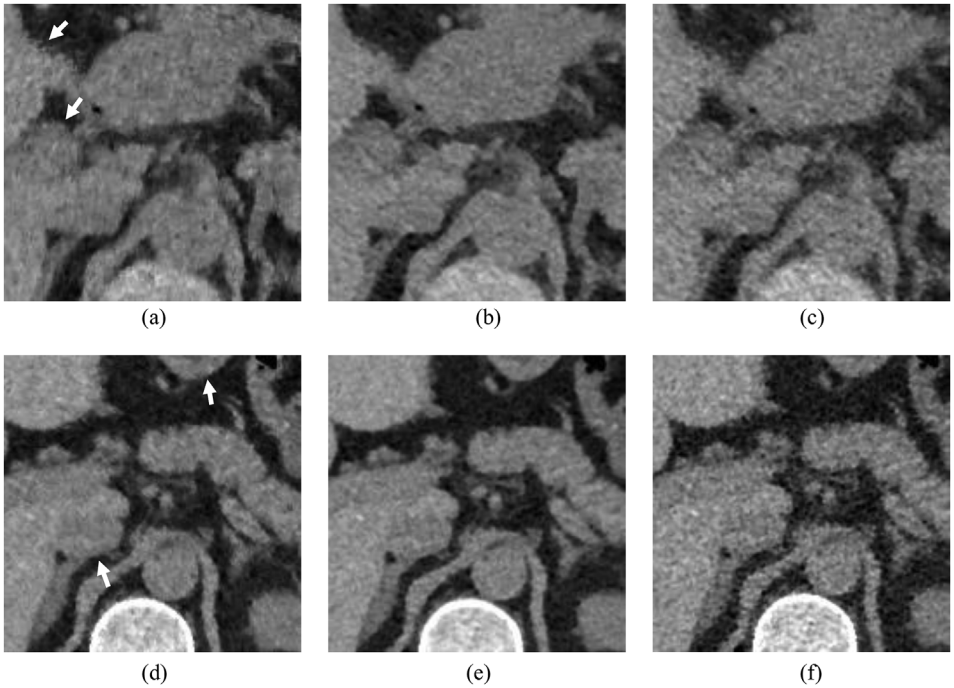

Fig. 9. Magnified images of the volunteer case 1 (a, b, c) and 2 (d, e, f), processed with (a, d) MBIR, (b, e) 3D-CDBF, and (c, f) 3D-BF. MBIR-processed images exhibited blush-like patterns (arrows), which substantially limited resolution.

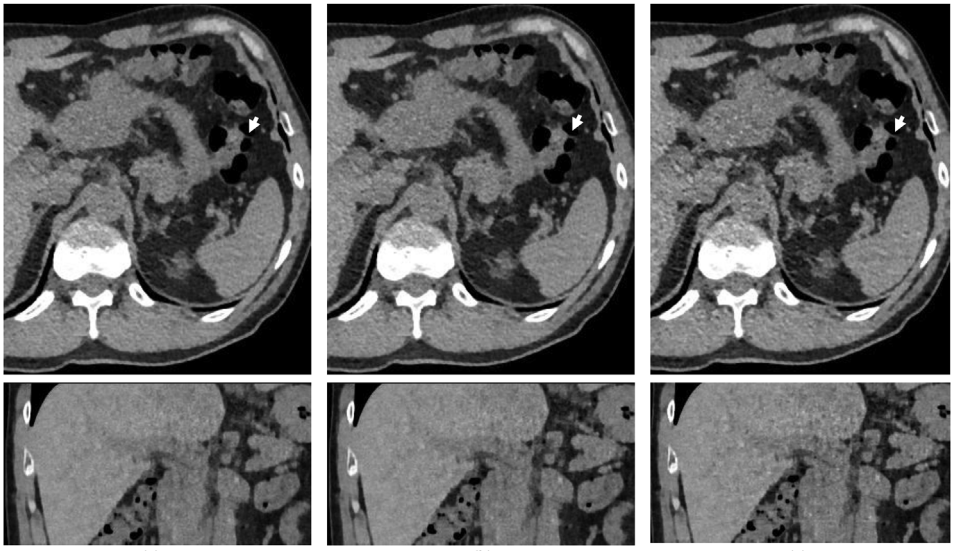

(a) (b) (c)

Fig. 11. Axial and coronal 3D-CDBF images with σ_{LPFp1} of (a) 6.0, (b) 3.0 (baseline), and (c) 1.5 for volunteer case 1.

acceptable signal-to-noise using low radiation doses as used in this study. In the volunteer cases, noise SD values were ~40 HU and image quality was significantly degraded by noise contamination using FBP (Figs. 7a and 8a). On the contrary, noise SD value was reduced to ~13 HU by MBIR, and MBIR with such thin slice thickness also yielded images in which 3D anatomical shapes were easily recognizable (Figs. 7b and 8b). These results are consistent with previous reports that presented high performances of the MBIR significantly superior to hybrid IR techniques at low doses of ~3 mGy [32,33]. Note that 3D-CDBF offered excellent noise reduction and edge preservation performances superior to MBIR (Figs. 7c, 8c, 9b and 9e). The abdominal vessels and thin walls of intestines were clearer than or similar to MBIR. Note that this improved performance was achieved through an image-based process rather than processing in projection space as is done with MBIR. Although the slice thickness (FWHM of SSP) was slightly broader than that of MBIR (0.99 mm for 3D-CDBF vs. 0.92 mm for MBIR), it was difficult to detect this difference in coronal images of volunteer cases.

As demonstrated in the phantom results and the abdominal images in Fig. 11, the initial LPF setting σ_{LPFp1} of cross-directional filtering was important for the speckle noise reduction, preserving object edges. Even with the largest σ_{LPFp1} (6.0), organ edges were observed similar to images with the lower σ_{LPFp1} (3.0 and 1.5) and the speckle noise was reduced sufficiently. However, the signal intensity reduction, as shown in Fig. 11a, was the drawback of the LPF use with an excessive low frequency response. σ_{LPFz2} (z-directional LPF at the final iteration) did not affect the noise and resolution properties and image appearance, as indicated in the phantom results and the abdominal images in Fig. 12. We presumed this is because image noise was sufficiently reduced in the first and second iterations; then, the bilateral filter in remaining iterations worked well without help of the z-directional LPF with large σ_{LPFz2}.

The 3D-CDBF method yielded significantly lower NPS values in the low-frequency range (up to 0.3 mm^{-1}) compared to MBIR. This superior low-frequency denoising was achieved by the z-directional bilateral filtering predominantly included in the first step of the iterative process in 3D-CDBF. In general, the NPS value at the lowest frequency is not altered by applying an in-plane LPF, but NPS decreases at higher spatial frequencies. On the other hand, a z-directional LPF reduces NPS over the entire frequency range, similar to an increase in radiation dose. Therefore, it was indicated that the MBIR was processed mostly in-plane because the NPS value at the lowest frequency (0.05 mm^{-1}) was close to that of FBP. In contrast, 3D-CDBF with the σ_{dz} parameter of 2.0 performed the filtering using four slices each above and below the target slice (a total of nine slices); thus, this reduces the image noise over the entire frequency range. Despite this z-directional processing, slice thickness was not broadened substantially compared to MBIR owing to the low σ_r of 10 HU for the range filtering required to properly detect object edges in the z-direction.

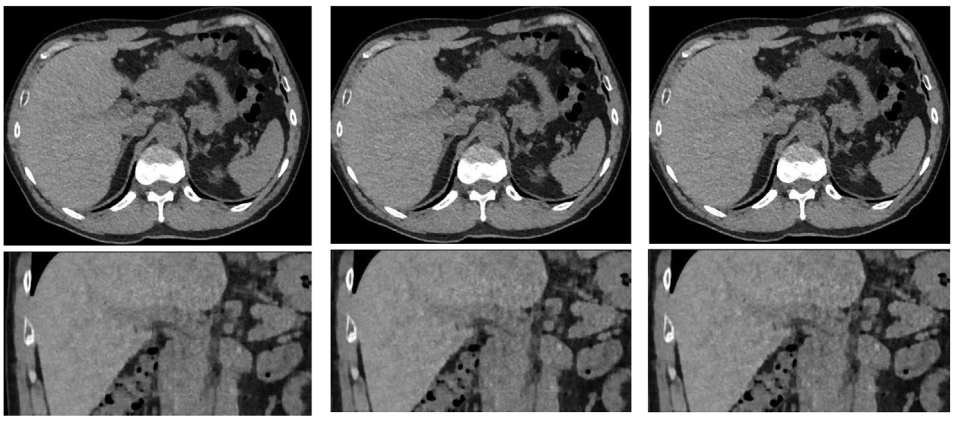

(a) (b) (c)

Fig. 12. Axial and coronal 3D-CDBF images with σ_{LPFz2} of (a) 3.0, (b) 1.5 (baseline), and (c) 0.75 for volunteer case 1.

The computation time of 3D-CDBF for a 3D data comprising 200 CT images was ~60 s for four iterations. This time was achieved by a program with a single thread on a computer system having Intel Core i7-7700 processor clocked at 3.6 GHz and was much shorter than the reconstruction time of MBIR (~30 min).

This study has certain limitations. The measured TTF was used only for the disk shape of 30-mm diameter. Although no shape dependency of TTF was reported in a previous study [22], the edge response for complicated shapes and signal losses at fine structures should be investigated using different phantoms or clinical cases. Furthermore, we evaluated CT images acquired at only one very low dose, 2.5 mGy, using a single CT system. Thus, the frequently used half and quarter doses should be included to examine whether 3D-CDBF can recover the half and quarter dose images to the same level of the routine dose using different CT systems. In addition, the baseline 3D-CDBF parameters we determined may not necessarily optimized ones for other CT systems even at the same low dose. As pointed out in a recent review [26], although image-based noise reduction techniques can be implemented across various CT scanner models, parameter selection for different types of images may still rely on trial-and-error adjustments to achieve a clinically acceptable image. As mentioned earlier, the contribution of each 3D-CDBF parameter is not difficult to understand; however, a more systematic method for optimization should be investigated.

In conclusion, we described an image-based edge-preserving noise reduction process using 3D cross-directional bilateral filtering, and demonstrated the superior denoising performance with improved edge preservation compared to MBIR, for low contrast (60 HU) phantom and real abdominal CT images at a low dose (2.5 mGy).

Funding statement

This research did not receive any specific grant from funding agencies in the public, commercial, or not-for-profit sectors.

Conflicts of interest

The authors declare that there are no competing interests.

References

[1] D.J. Brenner, E.J. Hall, Computed tomography: an increasing source of radiation exposure, N. Engl. J. Med. 357 (2007) 2277–2284.
[2] L.L. Geyer, U.J. Schoepf, F.G. Meinel, J.W. Nance Jr., G. Bastarrika, J.A. Leipsic, N.S. Paul, M. Rengo, A. Laghi, C.N. De Cecco, State of the art: iterative CT reconstruction techniques, Radiology 276 (2) (2015 Aug) 339–357, https://doi.org/10.1148/radiol.2015132766.
[3] M.J. Willemink, P.B. Noël, The evolution of image reconstruction for CT-from filtered back projection to artificial intelligence, Eur. Radiol. (2018 Oct 30), https://doi.org/10.1007/s00330-018-5810-7 [Epub ahead of print].
[4] F. Moloney, K. James, M. Twomey, D. Ryan, T.M. Grey, A. Downes, et al., Low-dose CT imaging of the acute abdomen using model-based iterative reconstruction: a prospective study, Emerg. Radiol. 26 (2) (2019) 169–177.
[5] A. Padole, S. Singh, J.B. Ackman, C. Wu, S. Do, S. Pourjabbar, et al., Submillisievert chest CT with filtered back projection and iterative reconstruction techniques, AJR Am. J. Roentgenol. 203 (4) (2014) 772–781.
[6] S. Pourjabbar, S. Singh, N. Kulkarni, V. Muse, S.R. Digumarthy, R.D. Khawaja, et al., Dose reduction for chest CT: comparison of two iterative reconstruction techniques, Acta Radiol. 56 (6) (2015) 688–695.
[7] H. Kawashima, K. Ichikawa, K. Matsubara, H. Nagata, T. Takata, S. Kobayashi, Quality evaluation of image-based iterative reconstruction for CT: comparison with hybrid iterative reconstruction, J. Appl. Clin. Med. Phys. 20 (6) (2019) 199–205, https://doi.org/10.1002/acm2.12597.
[8] J.M. Wolterink, T. Leiner, M.A. Viergever, I. Isgum, Generative adversarial networks for noise reduction in low-dose CT, IEEE Trans. Med. Imaging 36 (2017) 2536–2545.
[9] H. Chen, Y. Zhang, M.K. Kalra, F. Lin, Y. Chen, P. Liao, et al., Low-dose CT with a residual encoder-decoder convolutional neural network, IEEE Trans. Med. Imaging 36 (12) (2017) 2524–2535.
[10] M.J. Willemink, P.B. Noël, The evolution of image reconstruction for CT-from filtered back projection to artificial intelligence, Eur. Radiol. 29 (5) (2019) 2185–2195.
[11] A. Buades, B. Coll, J.M. Morel, A review of image denoising algorithms, with a new one, Multiscale Model. Simul. 4 (2005) 490–530.
[12] C. Tomasi, R. Manduchi, Bilateral filtering for gray and color images, IEEE Proc. Int. Conf. Comput. Vis. (1998) 839–846.
[13] Z. Li, L. Yu, J.D. Trzasko, D.S. Lake, D.J. Blezek, J.G. Fletcher, et al., Adaptive nonlocal means filtering based on local noise level for CT denoising, Med. Phys. 41 (1) (2014) 011908.
[14] H. Zhang, D. Zeng, J. Wang, Z. Liang, J. Ma, Applications of nonlocal means algorithm in low-dose X-ray CT image processing and reconstruction: a review, Med. Phys. 44 (3) (2017) 1168–1185.
[15] J.C. Giraldo, Z.S. Kelm, L.S. Guimaraes, L. Yu, J.G. Fletcher, B.J. Erickson, C.H. McCollough, Comparative study of two image space noise reduction methods for computed tomography: bilateral filter and nonlocal means, Conf. Proc. IEEE Eng. Med. Biol. Soc. 2009 (2009) 3529–3532.
[16] D. Bhonsle, V. Chandra, G.R. Sinha, Medical image denoising using bilateral filter, Int. J. Image Graph. Signal Process. 6 (2012) 36–43.
[17] I. Kumar, H.S. Bhadauria, J. Virmani, J. Rawat, Reduction of speckle noise from medical images using principal component analysis image fusion, Proceedings of International Conference on Industrial and Information Systems, IEEE press, New York, 2014, pp. 510–516 2014.
[18] G. Petschnigg, R. Szeliski, M. Agrawala, M. Cohen, H. Hoppe, K. Toyama, Digital photography with flash and no-flash image pairs, ACM Trans. Graph. 23 (3) (2004) 664–672.
[19] A.C. Martinsen, H.K. Sæther, P.K. Hol, D.R. Olsen, P. Skaane, Iterative reconstruction reduces abdominal CT dose, Eur. J. Radiol. 81 (7) (2012) 1483–1487.
[20] S. Singh, M.K. Kalra, J. Hsieh, P.E. Licato, S. Do, H.H. Pien, et al., Abdominal CT: comparison of adaptive statistical iterative and filtered back projection reconstruction techniques, Radiology 257 (2) (2010) 373–383.
[21] S. Richard, D.B. Husarik, G. Yadava, S.N. Murphy, E. Samei, Towards task-based assessment of CT performance: system and object MTF across different reconstruction algorithms, Med. Phys. 39 (7) (2012) 4115–4122.
[22] T. Takata, K. Ichikawa, W. Mitsui, H. Hayashi, K. Minehiro, K. Sakuta, et al., Object shape dependency of in-plane resolution for iterative reconstruction of computed tomography, Phys. Med. 33 (2017) 146–151.
[23] E. Samei, S. Richard, Assessment of the dose reduction potential of a model-based iterative reconstruction algorithm using a task-based performance metrology, Med. Phys. 42 (1) (2015) 314–323.
[24] A. Urikura, T. Hara, K. Ichikawa, E. Nishimaru, T. Hoshino, T. Yoshida, et al., Objective assessment of low-contrast computed tomography images with iterative reconstruction, Phys. Med. 32 (8) (2016) 992–998.
[25] IAEA, IAEA Safety Standards Series: Radiological Protection for Medical Exposure to Ionizing Radiation, No. RS-G-1.5, International Atomic Energy Agency, Vienna, 2002.
[26] E.C. Ehman, L. Yu, A. Manduca, A.K. Hara, M.M. Shiung, D. Jondal, et al., Methods for clinical evaluation of noise reduction techniques in abdominopelvic CT, Radiographics 34 (4) (2014) 849–862.
[27] L. Yu, T.J. Vrieze, S. Leng, J.G. Fletcher, C.H. McCollough, Technical Note: measuring contrast- and noise-dependent spatial resolution of an iterative reconstruction method in CT using ensemble averaging, Med. Phys. 42 (5) (2015) 2261–2267.
[28] E. Buhr, S. Günther-Kohfahl, U. Neitzel, Accuracy of a simple method for deriving the presampled modulation transfer function of a digital radiographic system from an edge image, Med. Phys. 30 (9) (2003) 2323–2331.
[29] B. Chen, O. Christianson, J.M. Wilson, E. Samei, Assessment of volumetric noise and resolution performance for linear and nonlinear CT reconstruction methods, Med. Phys. 41 (7) (2014) 071909.
[30] International Commission on Radiation Units and Measurements, Medical Imaging—The Assessment of Image Quality. ICRU Report No. 54, ICRU Publications, Bethesda, 1996.
[31] ICRP, The 2007 recommendations of the international commission on radiological protection ICRP Publication 103, Ann. ICRP 37 (2–4) (2007).
[32] P.A. Poletti, M. Becker, C.D. Becker, A. Halfon Poletti, O.T. Rutschmann, H. Zaidi, et al., Emergency assessment of patients with acute abdominal pain using low-dose CT with iterative reconstruction: a comparative study, Eur. Radiol. 27 (8) (2017) 3300–3309.
[33] Y. Jia, B. Zhai, T. He, Y. Yu, N. Yu, H. Duan, et al., The application of a new model-based iterative reconstruction in low-dose upper abdominal CT, Acad. Radiol. (2019), https://doi.org/10.1016/j.acra.2018.11.020 (Epub ahead of print), pii: S1076-6332(18)30539-7.